



Modelling, and characterization of 3D printed cellular structures

Michał Kucewicz ^a, Paweł Baranowski ^a, Jerzy Małachowski ^{a,*}, Arkadiusz Popławski ^a, Paweł Płatek ^b

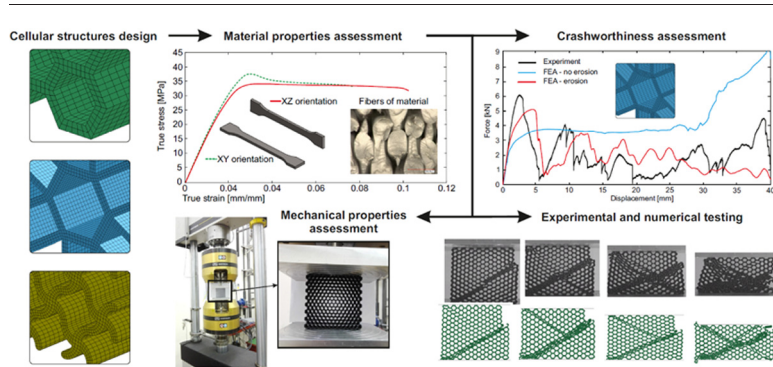
^a Military University of Technology, Faculty of Mechanical Engineering, Department of Mechanics and Applied Computer Science, 2 Gen. S. Kaliskiego Street, 00-908 Warsaw, Poland

^b Military University of Technology, Faculty of Mechatronics and Aviation, Institute of Armament Technology, 2 Gen. S. Kaliskiego Street, 00-908 Warsaw, Poland

HIGHLIGHTS

- Three different cellular structures are fabricated by FDM of ABSplus material
- Mechanical properties of the ABSplus material are determined
- Mesh sensitivity study is performed to assess the influence of mesh type and mesh size
- Crashworthiness properties of the three cellular structures are assessed during experimental and numerical testing

GRAPHICAL ABSTRACT



ARTICLE INFO

Article history:

Received 7 December 2017

Received in revised form 13 January 2018

Accepted 15 January 2018

Available online xxxx

Keywords:

3D printing

Cellular structure

Finite element modelling

Crashworthiness

Energy absorption

ABSTRACT

A procedure for characterizing the deformation process of a regular cellular structure under static loading conditions is presented. Three different topologies with similar relative densities were designed and fabricated by fused deposition modelling of ABSplus material. In the first stage, the material properties of the samples were evaluated and numerically correlated with experimental data. Experimental compression tests were performed on a universal strength machine. The comparison of the results of experiments and finite element analyses indicated acceptable similarity in terms of deformation, failure and force characteristics. Additionally, a mesh sensitivity study was performed, and the influence of the mesh on the obtained results was assessed. Finally, different types of elements for the discrete models of cellular structures were investigated. Two different approaches were considered for studying the energy-absorption properties of the cellular structures: with and without implementation of the erosion criterion for simulating material failure.

© 2018 Elsevier Ltd. All rights reserved.

1. Introduction

Advances in manufacturing technologies have led to increased interest in energy-absorbing structures [1–9]. In general, these structures are intentionally shaped elements fabricated from different types of

materials (e.g., metals, polymers, or foams) that are designed to disperse the maximum possible value of externally applied energy by transforming it to internal energy via deformation as plastic work. Consequently, energy-absorbing elements reduce the forces acting on the secured structures. These elements are mainly characterized by high deformability, plasticity and high ratios of stiffness to density and mass to density [10]. Due to their advantages, energy-absorbing structures are widely used in the military, transportation, aircraft and automotive industries. The geometrical features of a structure's topology strongly affect its crashworthiness behavior [2,7,11,12]. The most popular regular cellular structure topologies consist of elementary cells

* Corresponding author.

E-mail addresses: michał.kucewicz@wat.edu.pl (M. Kucewicz),
pawel.baranowski@wat.edu.pl (P. Baranowski), jerzy.malachowski@wat.edu.pl
(J. Małachowski), arkadiusz.poplawski@wat.edu.pl (A. Popławski),
pawel.platek@wat.edu.pl (P. Płatek).



periodically repeated and connected to each other. Irregular materials such as foams can also be considered as energy-absorbing elements in the engineering industry [13,14]. The revolution in additive manufacturing in combination with the increasing popularity of 3D printing and laser melting have enabled the fabrication of more complex, precise geometries [15–18] of energy-absorbing structures.

The crashworthiness of cellular structures can be investigated using analytical approaches [19–21], experimental techniques [3,6–8,17,22–26] and numerical simulations [4,22,27–29]. Analytical methodologies can be implemented for simple cellular topologies (e.g., circular, rectangular, triangle, hexagon) [17,22,24,30]. Experimental approaches provide accurate results [17,22,23,29,31–35] but are time-consuming and expensive, especially when metal or ceramic powder is used to manufacture the cellular structure samples. Numerical simulations are versatile and can be used to study complex cellular topologies [19,23,24,36]. Finite element analyses (FEA) can be adopted to predict the behavior and strength of structures within a wide range of strain rates [37–39]. However, for effective and correct analyses, a precise numerical model of the structure must be developed. The final form and properties of the finite element (FE) model are affected by many factors, and knowledge of the properties of the material is crucial for obtaining reliable results with good correspondence to the real-world structure [40–42].

Hu and Yu [21] conducted numerical simulations of a honeycomb cellular structure subjected to dynamic loading; in addition, the deformation process was validated and described analytically. In the authors' other studies [3,4], numerical and experimental results of quasi static compression tests of 3D printed samples fabricated from ABS were presented, and the influence of the relative density on the quantity of absorbed energy was discussed. These studies confirmed that finite element modeling (FEM) can be useful to simulate additively manufactured samples with good correlation with experimental results. Bates et al. [43] performed compression tests of functionally graded 3D printed structures of polyurethane and observed that the load plateau was nearly constant after initiation of plastic deformation for structures with constant wall thickness; by contrast, the load increased with displacement for walls of varied thickness. Habib et al. [44] have recently compared experimental, numerical and analytical results of compressive behavior of Nylon polymeric honeycombs fabricated by the FDM (fused deposition modelling) 3D printing technique. Other studies have demonstrated that 3D printing as well as numerical simulations are very useful in investigating cellular-like structures [27,28,45–47].

Different types of cellular structure topologies with negative stiffness have also been studied [48,49]. This type of structure can revert to its previous shape after deformation because the walls undergo elastic buckling rather than fracture. Another specific type of cellular structure is characterized by a negative Poisson's ratio [50–52]. For example, the use of two different materials for one structure in [50] yielded a stable negative Poisson's ratio even under large plastic deformation. Thus, structures with uniform geometry but varying auxetic properties can be produced.

The present paper is related to a recent project aimed at optimizing the crashworthiness behavior of regular cellular structures manufactured from Ti-6Al-4V alloy powder by LENS (Laser Engineered Net Shaping) [53] system under static and dynamic loading conditions. In this work, a comprehensive methodology is presented for the analysis of three different cellular structures fabricated from ABSplus material. The samples were first manufactured using rapid prototyping technology, followed by experimental tests of the material and correlation with modelling predictions and by quasi-static experimental compression tests with numerical simulations. Additionally, a sensitivity and parametric study was conducted to verify the influence of the applied mesh as well as the type of element on the obtained results. The correlation of the modelling and experimental results confirmed the effectiveness of the applied modelling method. Two different approaches were considered for studying the energy-absorption properties of the cellular structures: with and without implementation of the erosion criterion for simulating material failure.

The paper is organized as follows: in Section 2, the three cellular structures are introduced, and the material testing is described. In Section 3, the experimental and numerical compression tests are discussed, and the results of the mesh sensitivity and parametric studies are presented. Section 4 presents the results and discussion, and Section 5 provides the final conclusions.

2. Description of the cellular structures

Three different geometries of cell shapes were selected (Fig. 1). The assumptions underlying these geometries depend on the number of cells and technological possibilities of the implemented additive manufacturing system. The structures had cuboid-like geometries with dimensions of 80 × 80 × 20 mm (width x height x thickness) [3,4]. The honeycomb topology presented in Fig. 1a is a well-known and widely studied structure inspired by nature [1,23,44,54,55]. The second geometry was a modified honeycomb topology with spokes between adjacent cells, as shown in Fig. 1b. Such a geometry was selected, due to preliminary tests which showed that the structure may exhibit auxetic properties and it was assumed as an interesting case to be compared with the honeycomb topology. This phenomenon was not reproduced during experimental tests presented in Section 3 and Section 4, however it was included in the paper. The third topology, presented in Fig. 1c, had a spiral-like cellular geometry with a visible asymmetry which results in a different structure behavior during compression compared to the other two topologies. The second and third structures were designed by the authors. The cell wall thickness was chosen according to the assumption of an identical relative density (ratio of the volume of the structure to the volume of a cuboid with the same overall dimensions) of 35%.

A Dimension 1200es SST (Stratasys Corp.) 3D printer was used to manufacture the specimens and different cellular structure topologies using the FDM technique. ABSplus material commercially distributed by Stratasys Corp. was used. The parameters of the printing process were as follows: nozzle temperature, 300 °C; printing chamber temperature, 80 °C; single-layer thickness, approximately 0.3 mm. To maximize the mechanical properties of the samples, the type of fulfilment was set as "solid" in the software. These parameters are recommended by the manufacturer to obtain products of the best possible quality.

2.1. Acquisition of material data

Numerical calculations are effective tools to simulate physical phenomena. However, to predict the real behavior of structures under different loading conditions, constitutive models of the materials must be applied. Experimental tests were performed to determine the mechanical properties of the material used (i.e., ABSplus). Dog-bone specimens were prepared with dimensions according to the ASTM D638-14 standard [56]. A schematic of the specimen with marked dimensions is presented in Fig. 2, and the values of the corresponding dimensions are listed in Table 1. The mechanical properties of 3D printed materials are often strongly dependent on printing direction. Thus, samples printed in two orientations were analyzed in the tensile tests (Fig. 2).

Although the printer parameters were theoretically capable of producing solid, continuous structures, the specimens had empty spaces in their volume, particularly at the connection of the filling with the boundary layers. These pores directly reduced the strength of material, as discussed later in this section (please see Fig. 4). The mechanical properties of ABSplus provided by the manufacturer were measured for a specimen thickness of 2.5 mm, approximately 38% smaller than the specimen thickness used in the study. Reducing the thickness of the specimen to 1 mm could resolve this problem of material discontinuity. This reduced thickness reflects the technological limitations of the printer but can enable smooth and continuous printing of the material without additional layers differing in orientation and properties.

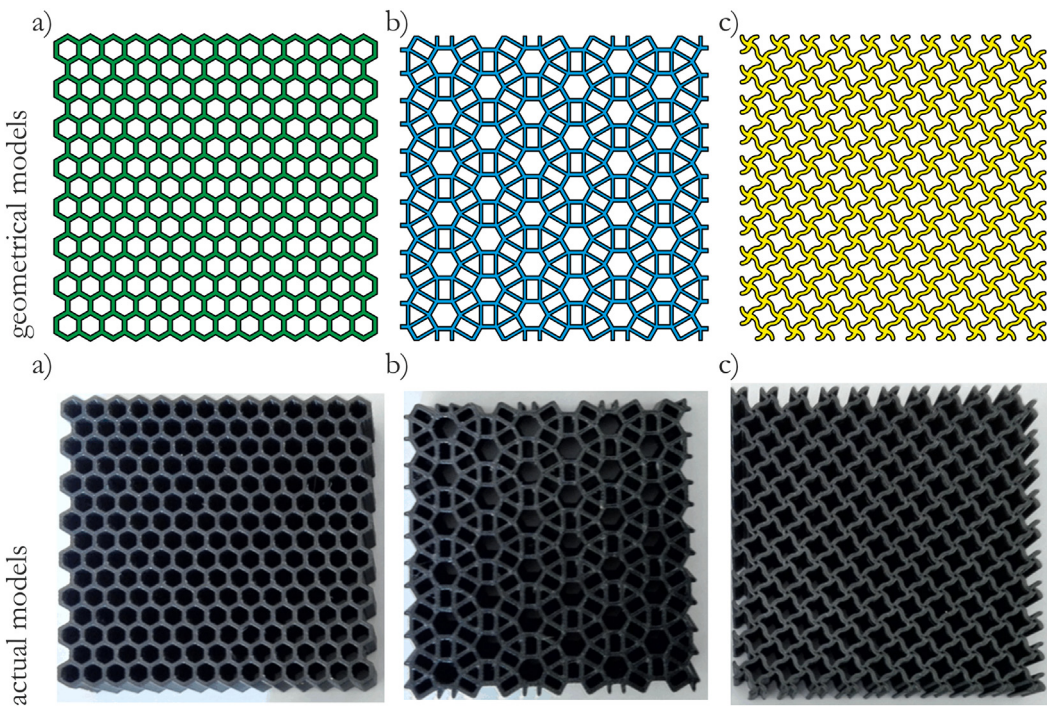


Fig. 1. The different topologies of the cellular structures used in this study (top, CAD models; bottom, printed structures): a) honeycomb, b) modified honeycomb, and c) spiral.

Uniaxial tensile tests were performed on an ElectroForce 3300 universal strength machine at a room temperature of 23 °C. The specimens were stretched at a velocity of 1 mm/s. Five specimens were used for each printing orientation. Based on the experimental tests, summary true stress vs. true strain curves were obtained for the specimens printed in the XZ and XY planes (Fig. 3). The profile of the curves differed depending on the printing orientation, considering differences in cross-sectional area. The specimens printed in the two directions had similar elastic ranges (slightly smaller in the XZ orientation). However, the stress value of the XZ orientation specimen decreased by approximately 5–7 MPa after reaching the maximum strength and persisted at the same level until failure. By contrast, the stress level of the XY orientation specimens remained constant until failure. Although the plastics did not have an apparent yield strength point due to their viscoplastic nature, it

can be observed the yield strength was larger for the XZ orientation than for the XY orientation. Moreover, opposing effects of print orientation on the failure strain value were observed.

The discrepancies between the two orientations can be explained based on observations of the specimens after the tests. Deformation of the specimens was observed within the whole measurement range, but plastic deformation occurred only in areas in which the filament in the inner part of the specimen was not connected with the boundary layers. To provide a better understanding of this phenomenon, the cross-sections of the specimens printed in two planes are presented in Fig. 4. Discontinuities (with an approximate dimension of 0.2–0.3 mm) in the border between the external and internal layers are clearly visible for the specimen printed in the XZ plane, and thus the inner and outer parts of the specimen were not connected. It is assumed that the

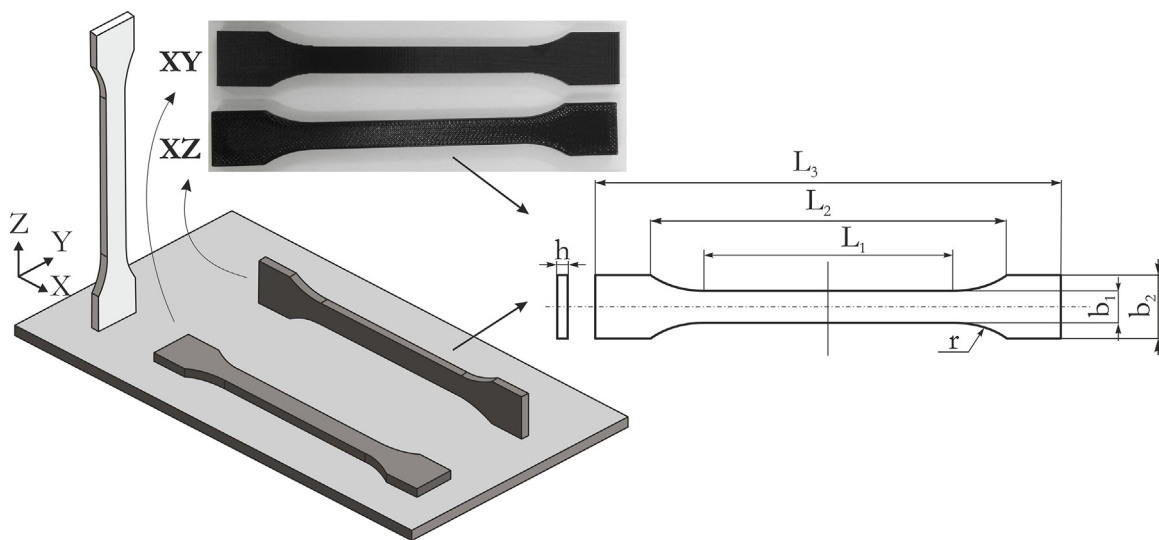


Fig. 2. Schematic of samples printed with the Dimension 1200es SST (Stratasys Corp.) 3D printer in two different printing orientations, and schematic of specimen for tensile tests according to the ASTM D638-14 standard [56].

Table 1

Specimen dimensions for tensile experimental tests (in mm).

L	L_1	L_2	L_3	L_0	r	h	b_1	b_2
115	80	115	130	50	20	4	10	20

greater damage in these areas is attributable to their lower strength. Consequently, the obtained mechanical properties of ABSplus are an underestimate, which must be taken into account to obtain the correct properties for a completely filled specimen. The approximate values of Young's modulus and the yield strength were also corrected based on the assumption of nonporous specimen material.

The strains measured during the experimental testing were larger than the values reported by the ABSplus manufacturer. This discrepancy was due to the discontinuities mentioned above, which allowed greater deformation of the specimen (by providing more space for internal deformation). This increased deformation could be avoided by reducing the thickness of the tested specimen to be equivalent to the thickness of the walls of the cellular structures. As shown in Fig. 4, the two printing orientations produced different filling characteristics. In both specimens, the path of the material was alternately arranged at an angle of 45° – 45° with respect to the central axis of geometry, but the specimens were printed in different planes. Consequently, the mechanical properties and modes of damage and crack propagation differed between the two specimens. These differences in filling characteristics resulted in a maximum strength deviation of 15%. Ultimately, the stress-strain curves of the two orientations were averaged such that the material itself was considered isotropic and was described using only one stress-strain curve. Moreover, when the printed cellular structures had a wall thickness of 1 mm, the problems of discontinuities and free-space areas were not observed. The mechanical properties obtained based on the experimental results were compared with the ABSplus data provided by the manufacturer (Table 2).

The comparison of the experimental mechanical data with the properties suggested by the manufacturer revealed that the scaling of the cross-section compensates for the difference in volume between fully and incompletely printed samples. The scaling also produces mechanical properties similar to the reference data. However, due to the differences in the cracking mechanism noted above, the calculated values of strain for fracture significantly differ from the reference data. In addition, the mechanical properties for bending reported by the manufacturer are considerably larger than the strength under tension. Therefore, it would be advisable to perform experimental bending tests of the material to evaluate its parameters under loading conditions other than uniaxial. Moreover, the material data provided by the manufacturer may differ by 15% depending on the batch of the product [57].

2.2. Constitutive model correlation

Before beginning the numerical simulation of the deformation process of the cellular structures, a constitutive material model that could properly predict the behavior of the cellular structure was selected. There are many well-known methods for modelling thermoplastics that can aid the simulation of elastic and plastic phases of deformation, including structure degradation and failure [58]. However, in this study, an elasto-plastic material model was used, in which the stress–plastic strain curve from the experimental tests was applied. During the FEA, the specimen was considered as continuous model without any discontinuities. Therefore, the stress–plastic strain curve was modified so that the yield stress was ~ 5% lower than the value obtained experimentally. Such an approach seems to be also justified by the results in other papers [59,60], where it was demonstrated that the point of yield for plastics should be measured for a smaller value of strain and it begins 5–10% earlier. In the subsequent stages of the study the erosion criterion was implemented to simulate structure destruction, based on the plastic strain failure variable taken from the quasi-static tension test [61]. The material properties were obtained from the ABSplus data provided by the manufacturer and from the experimental tests (Table 3). The points of the stress–plastic strain curve are shown in Table 4.

The selected constitutive model was correlated and tested under conditions corresponding to the experiments, and its ability to predict the response of the ABSplus material during quasi-static loading was investigated. Numerical simulations of the uniaxial tension test were performed using implicit LS-Dyna code and the Newton–Raphson iteration scheme [61], as described in a later section of the paper. For the quasi-static tests, an FE model consisting of 109,440 brick elements was used.

The curves from the actual and numerical tests are similar (Fig. 5), indicating that the selected constitutive model provides a correct representation of the ABSplus specimen response. The only difference is in the elastic range of the curve, which is perfectly linear in FEM and slightly non-linear in the actual test. The plastic deformation coincides well with the experimental results. Therefore, the constitutive material model was confirmed as correct and effective for use in further studies.

3. Experimental and numerical testing of cellular structures

3.1. Quasi-static experimental set-up

Uniaxial compression tests of the cellular structures were conducted with the same loading velocity used in the uniaxial tensile tests (1 mm/s) but on an INSTRON 8802 strength machine (Fig. 6). Each structure topology was compressed until reaching plastic deformation of 50%; beyond this point, the force increased rapidly, indicating densification of the structure. For each test, a fast Phantom V12 camera was used to record the deformation process of the structure.

3.2. Numerical modelling

Non-linear numerical studies of the deformation process of cellular structures were performed using LS-Dyna commercial code [61]. Because the aim was to analyze the influence of the numerical erosion consideration on the results, both implicit and explicit approaches were applied in the numerical studies. In implicit computations, the implementation of the erosion (deleting of elements) results in the formation of a large number of additional degrees of freedom at each time step, which is very problematic and time-consuming due to the need to compute and invert the stiffness matrix after each element is deleted.

In both methodologies, the two surfaces between which the structure was inserted were assumed to be non-deformable and were therefore represented by a rigid-wall model. The interaction between the FE cellular structure model and rigid walls was simulated using a contact procedure based on the penalty method with application of the Coulomb formulation to describe the tangential interaction between the

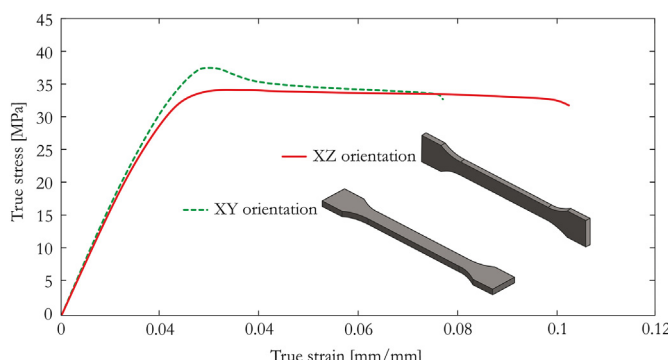


Fig. 3. Summary true stress – true strain curves for the tested ABSplus material.

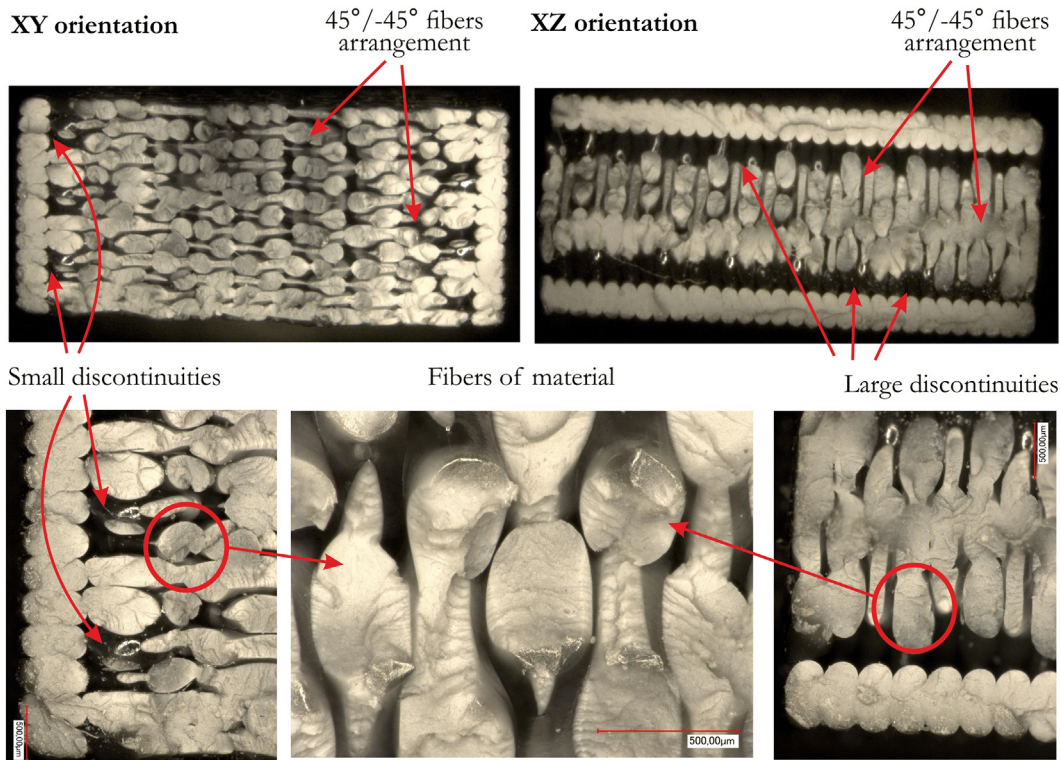


Fig. 4. Microscopic images of cross-sections of specimens printed in two directions.

bodies [61]. The friction mechanism plays a significant role in FE predictions of forces, and the friction coefficient is often used to readjust the forces obtained from numerical simulations. Thus, a number of simulations were performed with different friction coefficients; $\mu = 0.2$ gave force predictions closest to the experimental results and was therefore selected. The friction between the walls of the structure did not significantly affect the results, and therefore frictionless self-interaction was assumed between the structure cells.

Because the initial boundary conditions were identical for all cases, only a discrete model of the cellular honeycomb structure is presented in Fig. 7 for purposes of visualization.

3.2.1. Explicit simulation procedure

As mentioned before, the explicit approach was applied in order to consider the failure of material during simulating the deformation process of cellular structures. In general, the explicit dynamics procedure uses explicit central difference time integration, and the equation solved has the following form [61]:

$$\mathbf{M}\ddot{\mathbf{x}}_n = \mathbf{F}_n^{\text{ext}} - \mathbf{F}_n^{\text{int}} - \mathbf{C}\dot{\mathbf{x}}_n$$

Table 2
Material data for ABSplus and comparison with experimental data [57].

Material Parameter	Experiment	Manufacturer Data	Difference
Elastic modulus	2320 MPa	2200 MPa	5.2%
Tensile strength	35.5 MPa	33 MPa	7.1%
Yield strength	32 MPa	31 MPa	3.2%
Strain for fracture	8–9%	6%	2.5–3.3%
Strain at yield point	2.3%	2%	–13.1%
Bending strength	–	58 MPa	–
Flexural modulus	–	2100 MPa	–
Flexural strength	–	4%	–

where \mathbf{M} is a diagonal mass matrix; $\mathbf{F}_n^{\text{ext}}$ is external and body forces; $\mathbf{F}_n^{\text{int}}$ is a stress divergence vector; \mathbf{C} is a damping matrix; and $\mathbf{x}, \dot{\mathbf{x}}, \ddot{\mathbf{x}}$ are nodal displacement, velocity and acceleration vectors.

A solution of the above equation is obtained by numerical integration of acceleration $\ddot{\mathbf{x}}_n$ under the assumption that $\dot{\mathbf{x}} \approx \dot{\mathbf{x}}_{n-1/2}$

$$\ddot{\mathbf{x}}_n = \mathbf{M}^{-1} \left(\mathbf{F}_n^{\text{ext}} - \mathbf{C}\dot{\mathbf{x}}_{n-1/2} - \mathbf{F}_n^{\text{int}} \right)$$

which after implementation of the central difference equations for velocity and displacement yields the following:

$$\ddot{\mathbf{x}}_n = \frac{1}{\Delta t_n} \left(\dot{\mathbf{x}}_{n+1/2} - \dot{\mathbf{x}}_{n-1/2} \right) \Rightarrow \dot{\mathbf{x}}_{n+1/2} = \dot{\mathbf{x}}_{n-1/2} + \Delta t_n \ddot{\mathbf{x}}_n,$$

$$\dot{\mathbf{x}}_{n+1/2} = \frac{1}{\Delta t_{n+1/2}} (\mathbf{x}_{n+1} - \mathbf{x}_n) \Rightarrow \mathbf{x}_{n+1} = \mathbf{x}_n + \Delta t_{n+1/2} \dot{\mathbf{x}}_{n+1/2}.$$

The major advantage of this method is the lack of time-consuming operations involving stiffness matrix inversion. Instead, only a diagonal matrix of mass is inverted. However, the main disadvantage is that the method is conditionally stable and requires a time step to be limited

Table 3
Material properties of ABSplus used in FEA.

Material	Elastic modulus [MPa]	Poison's ratio [-]	Density [kg/m ³]	Yield stress [MPa]	Strain for fracture [%]
ABSplus	2200 ^a	0.35 ^a	1040 ^a	34.17 ^{b,c}	7.7 ^b

^a From manufacturer [57].

^b From experiments.

^c Modified values according to [59,60].

Table 4

Points of stress – plastic strain curve of ABSplus used in FEA.

Pl. strain value [%]	0.00	0.8	1.4	2.8	5.7	6.5	7.1	7.7
Stress value [MPa]	34.17	34.52	34.72	35.13	35.49	35.53	35.54	35.55

according to the Courant–Friedrichs–Lewy (CFL) stability condition [61],

$$\Delta t = \frac{L_E}{Q + \sqrt{Q^2 + c^2}}$$

where Q is the function of the viscous coefficients C_0 and C_1 and is formulated as follows:

$$Q = \begin{cases} C_1 c + C_0 L_E |\dot{\epsilon}_{kk}| & \text{for } \dot{\epsilon}_{kk} < 0 \\ 0 & \text{for } \dot{\epsilon}_{kk} \geq 0 \end{cases}$$

where $L_E = v_E/A_{E\max}$ is the characteristic length of the element, v_E is the volume of the element, $A_{E\max}$ is the largest side of the element area, and c is the adiabatic speed of sound.

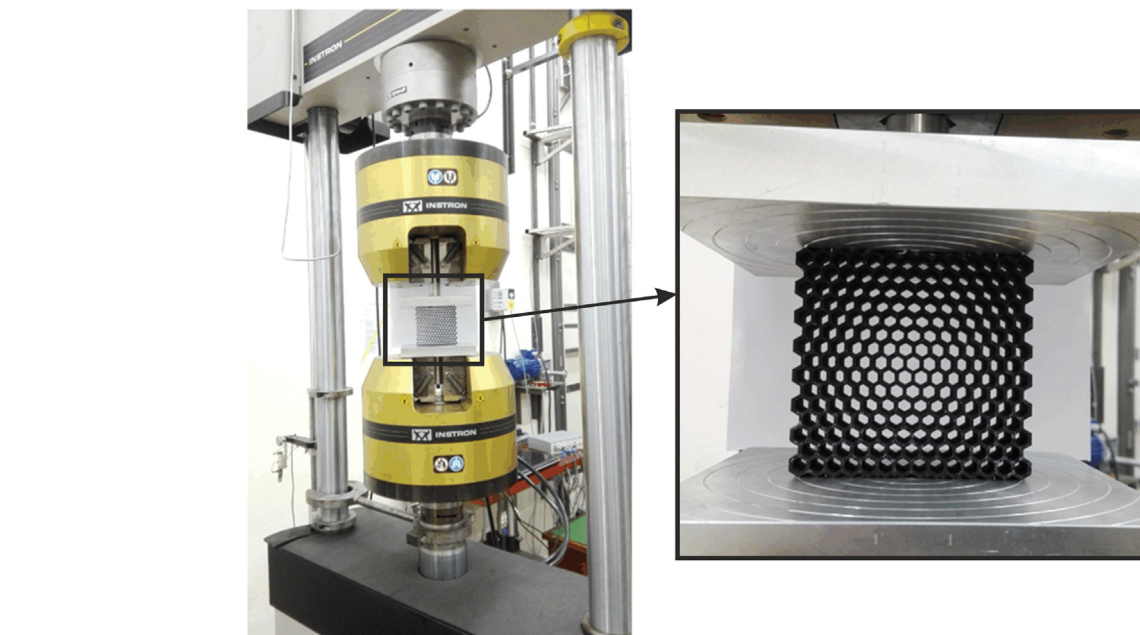


Fig. 6. Left, universal strength machine used in the experimental tests of the cellular structures; right, expanded view of the tested honeycomb structure.

To simulate structure destruction, the erosion criterion was implemented based on the effective strain failure variable taken from the quasi-static tension test [61].

The analyses were performed under a fully dynamic regime with direct integration in the time domain. To avoid unnecessary dynamics and to treat the analysis as quasi-static, the indenter had the following prescribed velocity [62,63]:

$$v(t) = \frac{\pi}{\pi - 2} \frac{s_{\max}}{T} \left[1 - \cos\left(\frac{\pi}{2T}t\right) \right]$$

where T is the total duration of loading and s_{\max} is the final displacement.

3.2.2. Implicit simulation procedure

Incremental static analyses (without the implementation of the erosion criterion) were performed using a full Newton–Raphson iteration scheme. The equation solved in this case had the following form [61]:

$$K_n \Delta n_{n+1} = F_{n+1}^{\text{ext}} - F_n^{\text{int}}$$

where K_n is the tangent stiffness matrix, Δn_{n+1} is the increment of the displacement vector, F_{n+1}^{ext} is the external and body force loads, and F_n^{int} is the stress divergence vector.

Convergence of the solution was controlled by two criteria: the relative displacement convergence tolerance $\varepsilon_{\text{disp}} = \|\Delta x^i\|/\Delta x_{\max} = 0.001$ and the relative energy convergence tolerance $\varepsilon_{\text{energ}} = |\Delta x^i Q^i|/|\Delta x^0 Q^0| = 0.01$, where $Q^i = F_i^{\text{ext}} - F_i^{\text{int}}$ and i is the implicit solver iteration.

3.2.3. Mesh sensitivity study

As noted previously, one of the main aims was to perform a sensitivity study of mesh density varying from coarse to fine (Table 5). For these analyses, the honeycomb cellular structure was chosen, and three different element types were analyzed, as shown in Fig. 8:

- (a) Brick elements (constant stress solid elements) with 8 nodes and one central integration point. Such elements are recommended for large deformation analyses [61,64]. Brick elements are efficient and accurate but require hourglass control in nearly every case.

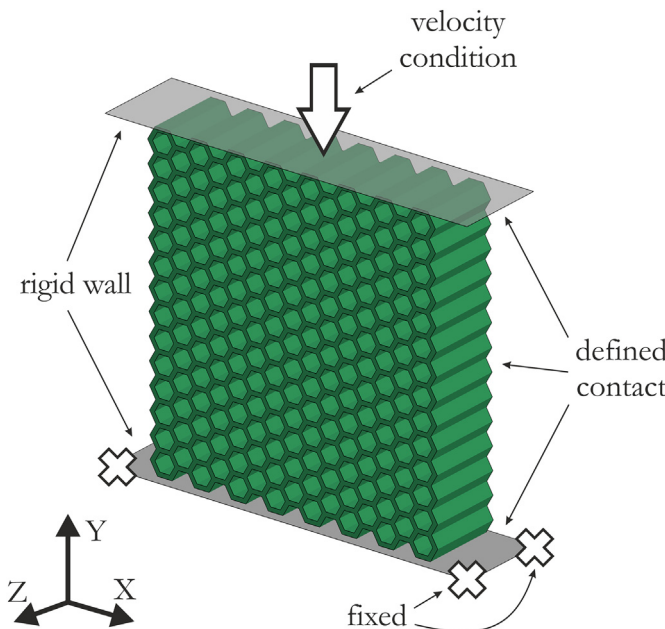


Fig. 7. Cellular structure for numerical analyses with applied initial boundary conditions.

(b) Belytschko-Tsay (BT) shell elements with 4 nodes and 5 integration points through the thickness. These shell elements have five integration points through the thickness and thus require only 725 mathematical operations, compared to 4050 for the integrated Hughes-Liu element (35,350 for the selectively reduced element) [61].

(c) Hughes-Liu beam elements with 2 nodes and 4 integration points (2×2), which are effective but simple and computationally efficient [61].

For each type of element, different mesh densities were examined to find an optimum dimension for the specified simulations (Fig. 8). Numerical erosion was not considered in the mesh sensitivity studies, and thus the implicit LS-Dyna code was adopted for the simulations.

The influence of mesh density was investigated by examining a measured force characteristic as a function of displacement. In each case, forces were taken from the interface between the rigid wall and the honeycomb structure. Based on the characteristics presented in Figs. 9–11, the absorbed energy and average force were calculated and compared (Table 6).

For the brick modelling (Fig. 9), using only one element (1.2 mm) through the thickness of the cell wall resulted in a decrease in structure stiffness, whereas using two elements through the thickness caused a

Table 5
Different element types and sizes considered in FEA.

Brick		Shell		Beam	
Elem. size [mm]	No. of elem. [-]	Elem. size [mm]	No. of elem. [-]	Elem. size [mm]	No. of elem. [-]
1.20	23,890	1.73	17,316	3.46	666
0.60	155,520	0.82	66,600	1.73	1332
0.40	387,868	0.48	131,868	0.86	1998
0.30	1,062,320	0.37	299,700	0.43	2664
0.24	1,238,880	0.28	535,464	0.35	3330

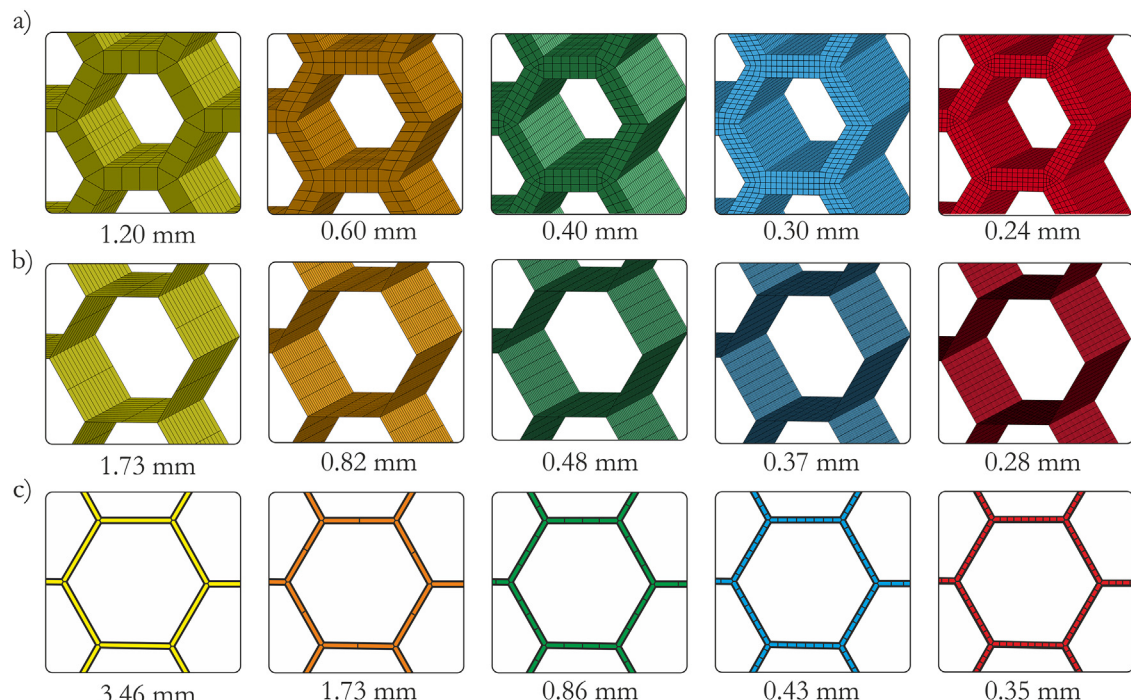


Fig. 8. Discrete honeycomb models using different types of elements: a) shells, b) bricks, and c) beams.

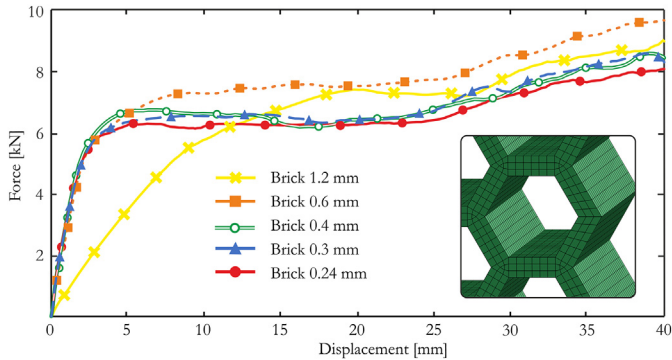


Fig. 9. Force vs. displacement curves for the honeycomb topology modelled using brick elements.

significant increase in stiffness (0.6 mm). Reducing the element size had little impact on the results, and the absorbed energy was similar for mesh sizes of 0.4 mm, 0.3 mm and 0.24 mm, with a value of $260 \text{ J} \pm 5\%$ (Table 6). Therefore, the model with three elements was considered reliable and produced satisfactory outcomes.

In Fig. 10, a similar comparison of results is presented for the simulations with shell modelling. The force was also estimated from the interface between the rigid walls and structure. An opposing influence of the mesh density on the results was observed. For the coarsest mesh (1.73 mm) with four elements on the cell wall, the force value appeared to be overestimated compared to the other meshes, resulting in the occurrence of the peak force after the elastic range. The obtained force values decreased as the characteristic length of the element was reduced. However, there was no significant difference between the models with element sizes of 0.37 mm and 0.28 mm (absorbed energy values of 219 J and 216 J respectively, a difference of 1.5% (Table 6)). The 0.37 mm mesh was able to represent the problem without a visible influence of element size. However, despite overestimating the maximum forces in the coarsest mesh modelling, the shell models gave approximately 25% smaller values of forces compared to the brick modelling.

The influence of mesh size was most apparent in the case of modelling the honeycomb structures using beam elements (Fig. 11). The coarsest mesh included only one element representing a single cell wall (3.46 mm). Surprisingly, for this mesh, a force peak was obtained at the initial stage of deformation, similar to the experimental results (see Fig. 14). However, erosion of the elements was not included in the discussed analyses, and therefore this force peak is assumed to be a result of the buckling of the elements representing the vertical cell walls. Reduction of the beam length eliminated the peak force simultaneous with a decrease in force and a plateau up to the maximum

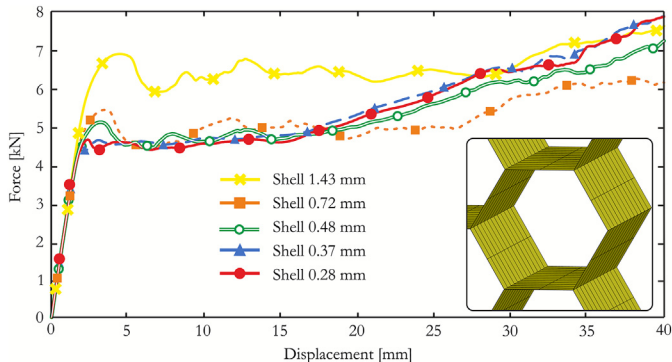


Fig. 10. Force vs. displacement curves for the honeycomb topology modelled using shell elements.

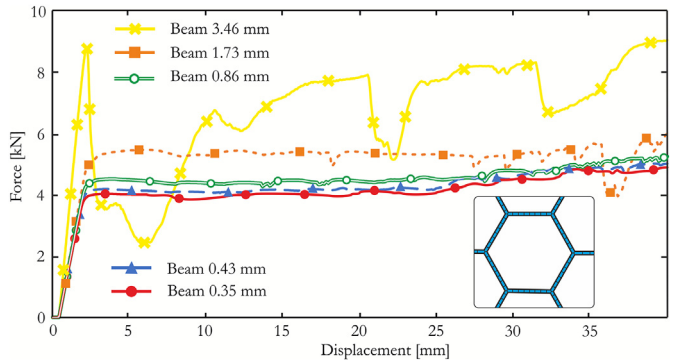


Fig. 11. Force vs. displacement curves for the honeycomb topology modelled using beam elements.

compression. A slight influence of mesh size was observed for models with six, eight and ten elements per cell wall. In these cases, the value of absorbed energy was 173 J, 167 J and 165 J, respectively (Table 6). The average force values were underestimated compared to the other two methods of modelling.

The influence of mesh size on the computational time is also evident. All simulations were carried using 24 Intel Xeon cores and Multi Parallel Processing (MPP) LS-Dyna code. In all cases the fine mesh increased computational time required to carry out simulation. The coarse mesh resulted in smaller number of elements and therefore in shorter simulation time. As expected, the longest simulations were observed with brick modelling, whereas the shortest computations were obtained with the FE models using beam elements. Simulations times for all considered cases are compared in Table 6.

In Fig. 12, the results for each FE case for which an influence of mesh was not apparent are compared with the actual tests. The result for the 0.4 mm case was selected for the brick modelling, 0.37 mm for the shell modelling, and 0.43 mm for the beam modelling. The rise times differed slightly from each other but were similar to the experimental elastic range, and therefore the stiffness of the material was correctly reflected in all models. The brick elements best represented the actual tests and therefore were selected for further modelling and simulations of the cellular structures.

3.2.4. Numerical model definition for quasi-static tests

In the next stage of the study, numerical simulations were performed for the three cellular structures presented in Section 2

Table 6

Comparison of the three implemented methods of modelling.

	Absorbed energy [J]	Average force [kN]	Simulation time [min]
Experiment	260.00	5.73	–
Brick model [mm]			
1.20	258.61	6.33	3.85
0.60	303.46	7.47	186.88
0.40	270.12	6.65	467.76
0.30	270.87	6.67	1144.53
0.24	260.03	6.35	2689.65
Shell model [mm]			
1.73	253.59	5.70	5.38
0.82	202.63	4.57	14.73
0.48	210.75	4.63	34.27
0.37	219.10	4.71	111.30
0.28	216.16	4.64	279.57
Beam model [mm]			
3.46	257.48	4.35	3.5
1.73	200.27	3.61	8.37
0.86	173.88	3.09	14.21
0.43	167.52	2.93	24.43
0.35	165.62	2.92	32.18

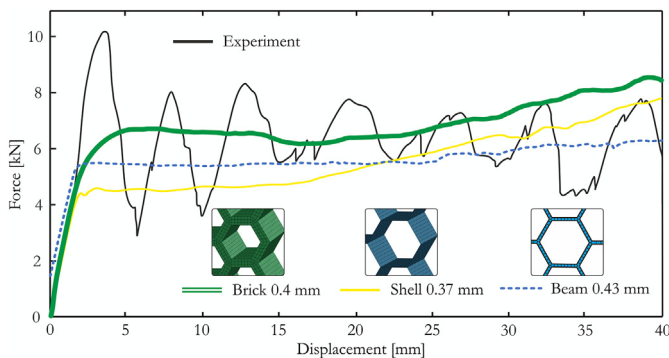


Fig. 12. Force vs. displacement from the experimental test and simulations using three different element types.

(Fig. 13). Based on the geometrical models, discrete models were developed, and the crashworthiness behavior of the analyzed structures subjected to a quasi-static compression load was predicted. The initial boundary conditions in FEA corresponded to the experiments and were identical to those in the mesh sensitivity analyses (see Fig. 7). Brick elements were adopted for the numerical representation of the structure. For all modified honeycomb and spiral structures, three elements were used to represent the thickness of the cell wall. In the honeycomb structure, only two elements were adopted, as will be explained later. In the spiral structure, some discontinuities were observed in the areas where the cell walls were connected due to differences in the thicknesses of the material single layer and the cell wall. The discontinuities were included in the discrete model as a hole with similar dimensions. To analyze the influence of the numerical erosion consideration on the results, implicit and explicit approaches were applied during the numerical studies.

4. Results and discussion

The relationship between force and displacement obtained from the numerical simulations was compared with the experimental results for each cellular structure as well as for the models with and without erosion. In Fig. 14, the results for the honeycomb structure are presented. The implicit and explicit analyses did not map an initial peak of force equal to 10 kN at the beginning of the deformation process. The maximum value obtained from the modelling with inclusion of the erosion criterion was 8 kN. Some oscillations related to differences between cells and their failure during self-interaction and interaction with the rigid wall were observed. The numbers of these rises and drops were identical between the actual and numerical tests with erosion. Although this characteristic was reproduced quite well, the obtained force values were still slightly lower than the experimentally determined values. This discrepancy may be attributable to the quasi-orthotropic behavior of ABSplus material. During the actual tests, only half of the wall was damaged at the beginning of structure compression, resulting in delamination of the two layers from which the single wall was built. Initially, three elements were considered to represent the cell walls during FEA,

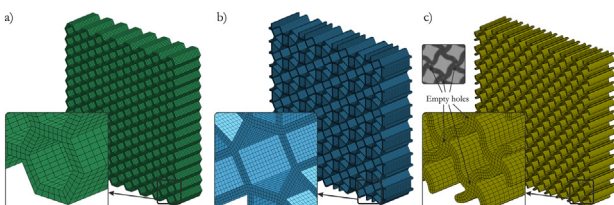


Fig. 13. Discrete models of energy-absorbing cellular structures.

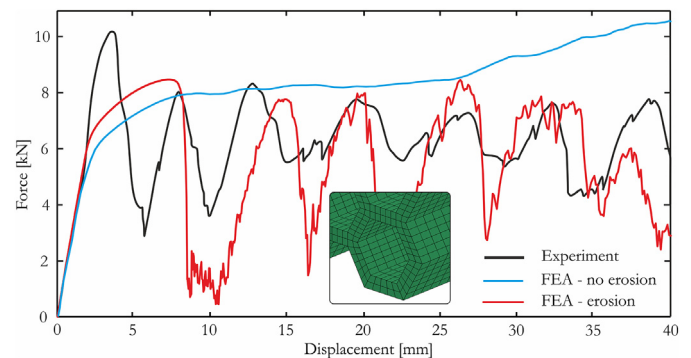


Fig. 14. Force vs. displacement from the experimental test and simulations of the honeycomb structure.

but this phenomenon was not reproduced in a satisfactory manner. Therefore, the FE model was simulated with two solid elements through the thickness, which significantly improved the results but resulted in a stiffer structure. The energy absorbed was also underestimated by 9.75% by the FE model of the honeycomb structure with erosion compared to the actual tests.

As expected, the behavior of the structure was not reproduced well in the implicit analysis adopting the constitutive model without consideration of the failure criterion. A plateau of force was observed throughout the whole duration of deformation. The value of absorbed energy was greater than for the explicit analysis and was far more to the experimental results, with a difference of 16.71%.

The results of the numerical simulations and experimental tests at the selected stages of the deformation processes of the honeycomb structure are shown in Fig. 15. The observed behaviors of the structure were quite similar, and the discrete model behaved correctly in all stages. The results are similar to those presented in the literature [3,4,44].

The second case, the modified honeycomb structure, was also simulated and tested under actual conditions. Fig. 16 presents the force versus displacement for the explicit, implicit and experimental tests. The fracture was more brittle in FEA of the modified honeycomb due to shearing damage of the walls (spokes) connecting adjacent cells. This result clearly demonstrates that for this structure the implemented isotropic elasto-plastic material model is insufficient and requires the inclusion of additional material properties related to the bending response. However, the general behavior of the model, including failure, was well reproduced. Fig. 17 presents the deformation process at selected stages of the experimental and numerical tests. Due to visible damage, the modified honeycomb structure separated into three triangular-like parts, and this separation was also reproduced quite well using FEA.

In the model without the failure force-displacement relationship differed significantly from the experimental curve. In addition to overestimating the forces, a plateau was observed. Moreover, the force increased suddenly at the end of the deformation due to structure densification.

For the last structure (spiral), the characteristics of the force vs. displacement curve differed from the previous two cases (Fig. 18). Implementing the erosion criterion improved the reproduction of the force characteristics, even though only a few elements were deleted from the model. However, these deleted elements were removed from crucial areas of the structure and thus impacted its stiffness. The failure of the model also resulted in reasonable agreement between the numerical and experimental values of absorbed energy, with a difference of 8.7% compared to 25.9% in the implicit case. The superior reproduction of the spiral structure behavior by the constitutive material model with the erosion criterion is also confirmed in Fig. 19, which shows the results of the numerical simulations and actual tests at selected

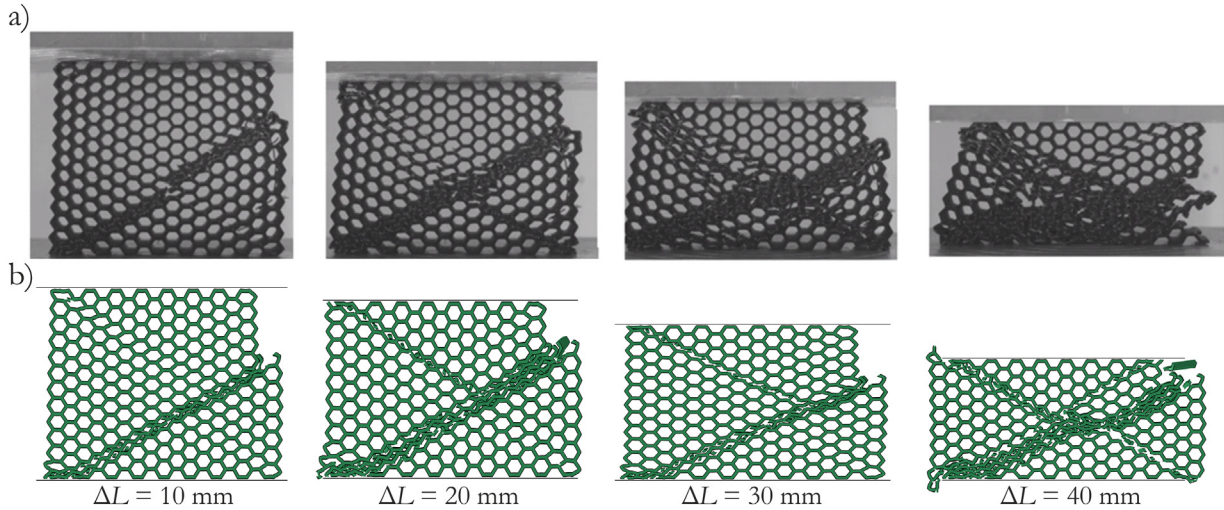


Fig. 15. Successive stages of deformation of the honeycomb structure: a) experiment, b) FEA.

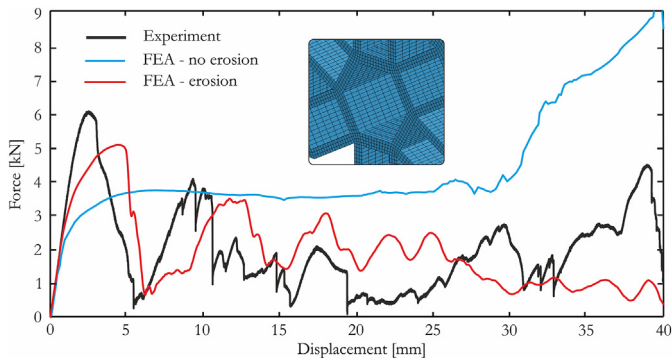


Fig. 16. Force vs. displacement from the experimental test and simulations of the modified honeycomb structure.

stages of the deformation processes. Comparing the behaviors of the spiral structure and the honeycomb structure reveals a similar profile: after overcoming the yield strength, oscillations occurred in the plateau region due to failure and cracking of the cell walls.

To determine which structure was the most efficient in terms of energy-absorption capabilities, the values of absorbed energy were compared as presented in **Table 7**. The average force and computational

times are also included in **Table 7** for comparison purposes. In every case, the value of absorbed energy obtained from the implicit simulations was larger than the actual value. This discrepancy is attributable to the greater stiffness of the model in which no element deletion was assumed, even after reaching the failure strain value. For the honeycomb structure, this difference was relatively small; however, the characteristics of the obtained force-displacement curve were significantly different. With implementation of the numerical erosion criterion, the value of the absorbed energy decreased compared to the implicit cases, and a larger difference was observed for the modified honeycomb structure. The honeycomb structure clearly had the best energy-absorption capabilities as it consumed larger values of energy compared to the other two topologies. In the modified honeycomb this is a result of brittle fracture and shearing damage in parallel spokes connecting adjacent cells. On the other hand, the asymmetry of the spiral geometry resulted in a leaning of the specimen influencing its stiffness and consequently its energy-absorption capabilities.

5. Conclusions

This paper presents experimental and numerical studies of the deformation process of 3D printed cellular structures under uniaxial compression loading. One of the main aims of this study was to perform a mesh sensitivity study to assess the influence of the mesh size the

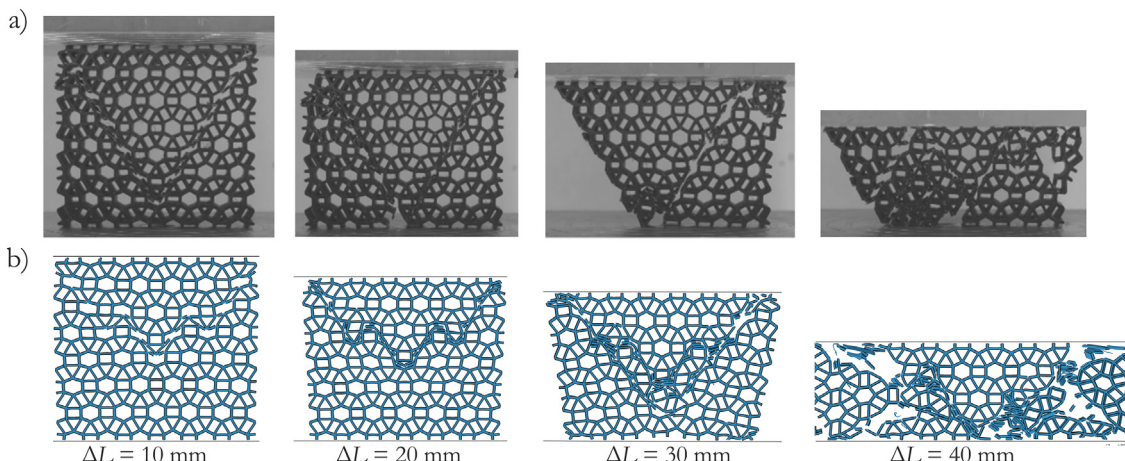


Fig. 17. Successive stages of deformation of the modified honeycomb structure: a) experiment, b) FEA.

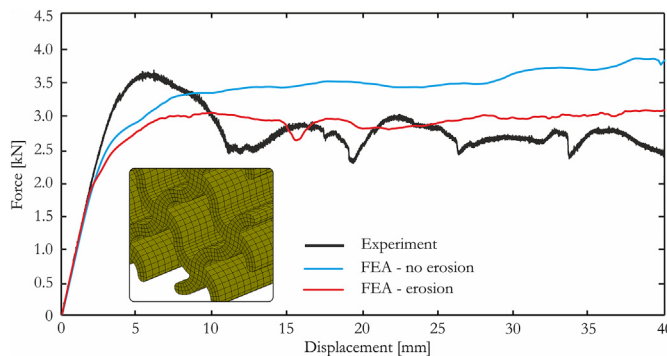


Fig. 18. Force vs. displacement from the experimental test and simulations of the spiral structure.

obtained results. Additionally, different types of elements, i.e., brick, shell and beam elements, were investigated and compared.

Based on the results, the following conclusions can be drawn:

- The adopted mesh size influenced the results observed for each cellular structure. In each method of modelling (brick, shell and beam), the lowest values of force were obtained with finer mesh. The influence of mesh size was most apparent in the simulations using beam elements.
- The elasto-plastic material with the failure criterion based on the plastic strain value adopted in FEA was adequate for simulating the deformation process of the cellular structures manufactured using FDM technology. However, to consider discontinuities in the

material or delamination of the printed layers, it may be necessary to implement meshless methods of modelling or orthotropic properties of the material, respectively. The present study represents a compromise between simulations at the microscopic and macroscopic levels that allowed the results to be verified using available experimental data. Although simulating the problem at the micro-level using a very fine mesh would allow a single layer of the material to be represented, but it was not the objective of this paper.

- The most desirable characteristic of cellular materials is a long plateau region in the stress-strain curve. This property was obtained for the spiral structure, in which failure of the material did not result in oscillations of the curve, in contrast to the honeycomb structure. According to the results presented in Table 7, the honeycomb structure has the best energy-absorption and crashworthiness properties.

In future studies, an advanced additive manufacturing LENS system will be implemented for manufacturing regular cellular structures from Ti-6Al-4V. Moreover, the investigations will be extended to analyze the structures under dynamic loading conditions as well as the effect of the strain rate. An optimization procedure based on genetic algorithms is planned to find the optimum topology in terms of crashworthiness and energy-absorption capabilities.

Acknowledgements

The research was supported by the National Science Centre under research grant no. 2015/17/B/ST8/00825 and the Interdisciplinary Centre for Mathematical and Computational Modeling (ICM), University of Warsaw, under grant no GB65-19.

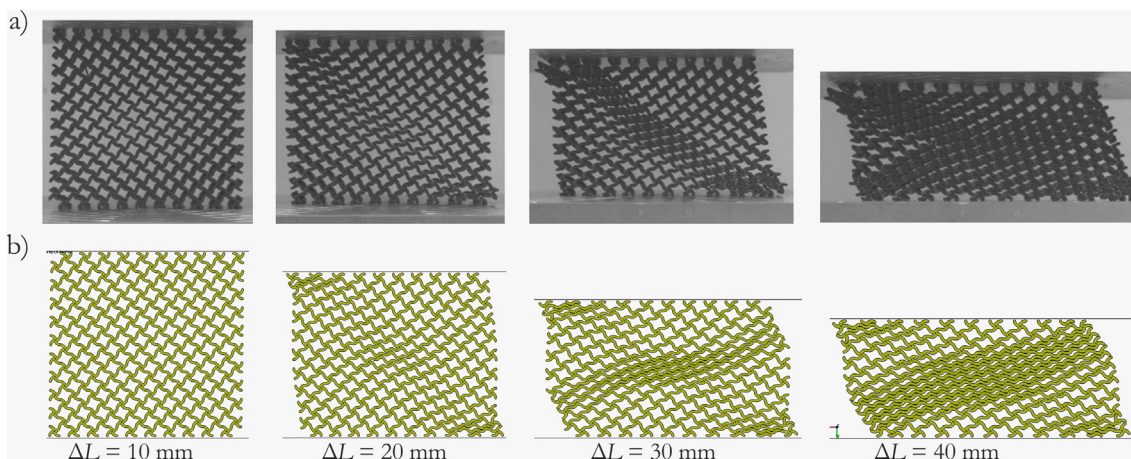


Fig. 19. Successive stages of deformation of the spiral structure: a) experiment, b) FEA.

Table 7
Comparison of the three cellular structures.

Type of structure		Absorbed energy [J]	Average force [kN]	Absorbed energy % of experimental result	Average force % of experimental result	Simulation time [min]
Honeycomb	Experiment	260.00	5.73	100.00	100.00	–
	Implicit	303.46	6.73	116.71	117.45	467.76
	Explicit	234.67	6.06	90.25	105.76	388.93
Modified Honeycomb	Experiment	79.12	1.77	100.00	100.00	–
	Implicit	175.33	4.76	221.47	268.93	788.65
	Explicit	59.36	1.75	75.12	98.87	674.06
Spiral	Experiment	105.69	2.64	100.00	100.00	–
	Implicit	133.14	3.72	125.95	140.91	628.37
	Explicit	114.89	3.04	108.71	115.15	544.40

References

- [1] L. Gibson, M. Ashby, *Cellular Materials: Structure and Properties*, 1988.
- [2] A. Ajdari, H. Nayeb-Hashemi, A. Vaziri, Dynamic crushing and energy absorption of regular, irregular and functionally graded cellular structures, *Int. J. Solids Struct.* 48 (2011) 506–516, <https://doi.org/10.1016/j.ijsolstr.2010.10.018>.
- [3] P. Dziewit, P. Platek, J. Janiszewski, M. Sarzyński, M. Grązka, R. Paszkowski, in: S. Gomes, S.A. Meguid (Eds.), *Mechanical Response of Additive Manufactured Regular Cellular Structures in Quasi-static Loading Conditions - Part II Numerical Investigations*, Proc. 7th Int. Conf. Mech. Mater. Des., Albufeira, 2017, pp. 1074–1090.
- [4] P. Dziewit, P. Platek, J. Janiszewski, M. Sarzyński, M. Grązka, R. Paszkowski, in: S. Gomes, S.A. Meguid (Eds.), *Mechanical Response of Additive Manufactured Regular Cellular Structures in Quasi-static Loading Conditions - Part I Experimental Investigations*, Proc. 7th Int. Conf. Mech. Mater. Des., Albufeira, 2017, pp. 1061–1074.
- [5] A.G. Evans, J.W. Hutchinson, N.A. Fleck, M.F. Ashby, H.N.G. Wadley, The topological design of multifunctional cellular metals, *Prog. Mater. Sci.* 46 (2001) 309–327, [https://doi.org/10.1016/S0079-6425\(00\)00016-5](https://doi.org/10.1016/S0079-6425(00)00016-5).
- [6] M. Bodaghi, A.R. Damanpack, G.F. Hu, W.H. Liao, Large deformations of soft metamaterials fabricated by 3D printing, *Mater. Des.* 131 (2017) 81–91, <https://doi.org/10.1016/j.matdes.2017.06.002>.
- [7] V.J. Challis, X. Xu, L.C. Zhang, A.P. Roberts, J.F. Grotowski, T.B. Sercombe, High specific strength and stiffness structures produced using selective laser melting, *Mater. Des.* 63 (2014) 783–788, <https://doi.org/10.1016/j.matdes.2014.05.064>.
- [8] S.Y. Choy, C.-N. Sun, K.F. Leong, J. Wei, Compressive properties of functionally graded lattice structures manufactured by selective laser melting, *Mater. Des.* 131 (2017) 112–120, <https://doi.org/10.1016/j.matdes.2017.06.006>.
- [9] N. Tanlak, D.F. De Lange, W. Van Paepengen, Numerical prediction of the printable density range of lattice structures for additive manufacturing, *Mater. Des.* 133 (2017) 549–558, <https://doi.org/10.1016/j.matdes.2017.08.007>.
- [10] M.F. Ashby, The mechanical properties of cellular solids, *Metall. Trans. A* 14 (1983) 1755–1769, <https://doi.org/10.1007/BF02645546>.
- [11] X. Huang, Y.M. Xie, Optimal design of periodic structures using evolutionary topology optimization, *Struct. Multidiscip. Optim.* 36 (2008) 597–606, <https://doi.org/10.1007/s00158-007-0196-1>.
- [12] F. Sun, C. Lai, H. Fan, In-plane compression behavior and energy absorption of hierarchical triangular lattice structures, *Mater. Des.* 100 (2016) 280–290, <https://doi.org/10.1016/j.matdes.2016.03.023>.
- [13] Ł. Mazurkiewicz, J. Małachowski, P. Baranowski, Optimization of protective panel for critical supporting elements, *Compos. Struct.* 134 (2015) 493–505, <https://doi.org/10.1016/j.compstruct.2015.08.069>.
- [14] R. Panowicz, D. Miedzińska, Numerical and experimental research on polyisocyanurate foam, *Comput. Mater. Sci.* 64 (2012) 126–129, <https://doi.org/10.1016/j.commatsci.2012.05.069>.
- [15] B. Haghpanah, J. Papadopoulos, D. Mousanezhad, H. Nayeb-Hashemi, A. Vaziri, Buckling of regular, chiral and hierarchical honeycombs under a general macroscopic stress state, *Proc. R. Soc. Lond. A Math. Phys. Sci.* 470 (2014), 20130856, <https://doi.org/10.1098/rspa.2013.0856>.
- [16] F. Brenne, T. Niendorf, H.J. Maier, Additively manufactured cellular structures: impact of microstructure and local strains on the monotonic and cyclic behavior under uniaxial and bending load, *J. Mater. Process. Technol.* 213 (2013) 1558–1564, <https://doi.org/10.1016/j.jmatprotec.2013.03.013>.
- [17] C. Yan, L. Hao, A. Hussein, D. Raymont, Evaluations of cellular lattice structures manufactured using selective laser melting, *Int. J. Mach. Tools Manuf.* 62 (2012) 32–38, <https://doi.org/10.1016/j.ijmachtools.2012.06.002>.
- [18] L. Xiao, W. Song, Additively-manufactured functionally graded Ti-6Al-4V lattice structures with high strength under static and dynamic loading: experiments, *Int. J. Impact Eng.* 111 (2018) 255–272, <https://doi.org/10.1016/j.ijimpeng.2017.09.018>.
- [19] A.P. Roberts, E.J. Garboczi, Elastic properties of model random three-dimensional open-cell solid, 50 (2002) 33–55, [https://doi.org/10.1016/S0022-5096\(01\)00056-4](https://doi.org/10.1016/S0022-5096(01)00056-4).
- [20] M. Eidini, Zigzag-base folded sheet cellular mechanical metamaterials, *Extrem. Mech. Lett.* 6 (2016) 96–102, <https://doi.org/10.1016/j.eml.2015.12.006>.
- [21] L.L. Hu, T.X. Yu, Dynamic crushing strength of hexagonal honeycombs, *Int. J. Impact Eng.* 37 (2010) 467–474, <https://doi.org/10.1016/j.ijimpeng.2009.12.001>.
- [22] S.L. Campanelli, N. Contuzzi, A.D. Ludovico, F. Caiazzo, F. Cardaropoli, V. Sergi, Manufacturing and characterization of Ti₆Al₄V lattice components manufactured by selective laser melting, *Materials* 7 (2014) 4803–4822, <https://doi.org/10.3390/ma7064803>.
- [23] D. Restrepo, N.D. Mankame, P.D. Zavattieri, Programmable materials based on periodic cellular solids. Part I: experiments, *Int. J. Solids Struct.* 100–101 (2016) 485–504, <https://doi.org/10.1016/j.ijsolstr.2016.09.021>.
- [24] K. Tantikom, T. Aizawa, Compressive deformation simulation of regularly cell-structured materials with various column connectivity, *Mater. Trans.* 46 (2005) 1154–1160, <https://doi.org/10.2320/matertrans.46.1154>.
- [25] Q. Ma, H. Cheng, K.I. Jang, H. Luan, K.C. Hwang, J.A. Rogers, Y. Huang, Y. Zhang, A nonlinear mechanics model of bio-inspired hierarchical lattice materials consisting of horseshoe microstructures, *J. Mech. Phys. Solids* 90 (2016) 179–202, <https://doi.org/10.1016/j.jmps.2016.02.012>.
- [26] F. Sun, C. Lai, H. Fan, In-plane compression behavior and energy absorption of hierarchical triangular lattice structures, *Mater. Des.* 100 (2016) 280–290, <https://doi.org/10.1016/j.matdes.2016.03.023>.
- [27] X. Zhang, L. An, H. Ding, Dynamic crushing behavior and energy absorption of honeycombs with density gradient, *J. Sandw. Struct. Mater.* 16 (2014) 125–147, <https://doi.org/10.1177/1099636213509099>.
- [28] M.R. Karamooy Ravari, M. Kadkhodaei, M. Badrossamay, R. Rezaei, Numerical investigation on mechanical properties of cellular lattice structures fabricated by fused deposition modeling, *Int. J. Mech. Sci.* 88 (2014) 154–161, <https://doi.org/10.1016/j.ijmecsci.2014.08.009>.
- [29] Z. Ozdemir, A. Tyas, R. Goodall, H. Askes, Energy absorption in lattice structures in dynamics: nonlinear FE simulations, *Int. J. Impact Eng.* 102 (2017) 1–15, <https://doi.org/10.1016/j.ijimpeng.2016.11.016>.
- [30] S. Babaee, B.H. Jahromi, A. Ajdari, H. Nayeb-Hashemi, A. Vaziri, Mechanical properties of open-cell rhombic dodecahedron cellular structures, *Acta Mater.* 60 (2012) 2873–2885, <https://doi.org/10.1016/j.actamat.2012.01.052>.
- [31] D. Prall, R.S. Lakes, Properties of a chiral honeycomb with a poisson's ratio of −1, *Int. J. Mech. Sci.* 39 (1997) 305–307.
- [32] S. Nemat-Nasser, W.J. Kang, J.D. McGee, W.G. Guo, J.B. Isaacs, Experimental investigation of energy-absorption characteristics of components of sandwich structures, *Int. J. Impact Eng.* 34 (2007) 1119–1146, <https://doi.org/10.1016/j.ijimpeng.2006.05.007>.
- [33] C. Yan, L. Hao, A. Hussein, P. Young, D. Raymont, Advanced lightweight 316L stainless steel cellular lattice structures fabricated via selective laser melting, *Mater. Des.* 55 (2014) 533–541, <https://doi.org/10.1016/j.matdes.2013.10.027>.
- [34] M. Leahy, M. Mazur, J. Elambasseri, M. McMillan, T. Chirent, Y. Sun, M. Qian, M. Easton, M. Brandt, Selective laser melting (SLM) of AlSi12Mg lattice structures, *Mater. Des.* 98 (2016) 344–357, <https://doi.org/10.1016/j.matdes.2016.02.127>.
- [35] Y. Sun, Q.M. Li, Dynamic compressive behaviour of cellular materials: a review of phenomenon, mechanism and modelling, *Int. J. Impact Eng.* 112 (2018) 74–115, <https://doi.org/10.1016/j.ijimpeng.2017.10.006>.
- [36] J. Bauer, S. Hengsbach, I. Tesari, R. Schwaiger, O. Kraft, High-strength cellular ceramic composites with 3D microarchitecture, *Proc. Natl. Acad. Sci. U. S. A.* 111 (2014) 2453–2458, <https://doi.org/10.1073/pnas.1315147111>.
- [37] G. Slawinski, T. Niezgoda, Protection of occupants military vehicles against mine threats and improvised explosive devices (IED) |Ochrona Zalogi Pojazdu Wojskowego Przed Wybuchem Min I Improwizowanymi Anykami Wybuchowymi (IED), *J. Konbin.* 33 (2015) 123–134, <https://doi.org/10.1515/jok-2015-0009>.
- [38] P. Kedzierski, R. Gieleta, A. Morka, T. Niezgoda, Z. Surma, Experimental study of hybrid soft ballistic structures, *Compos. Struct.* 153 (2016) 204–211, <https://doi.org/10.1016/j.compstruct.2016.06.006>.
- [39] P. Baranowski, J. Małachowski, Numerical study of selected military vehicle chassis subjected to blast loading in terms of tire strength improving, *Bull. Polish Acad. Sci. Tech. Sci.* 63 (2015) 867–878, <https://doi.org/10.1515/bpasts-2015-0099>.
- [40] P. Mayer, D. Pyka, K. Jamroziak, J. Pach, M. Bocian, Experimental and numerical studies on ballistic laminates on the polyethylene and polypropylene matrix, *J. Mech.* (2017) 1–11, <https://doi.org/10.1017/jmech.2017.103>.
- [41] P. Rozyro, H. Dębski, T. Kubiak, A model of low-velocity impact damage of composite plates subjected to compression-after-impact (CAI) testing, *Compos. Struct.* 181 (2017) 158–170, <https://doi.org/10.1016/j.compstruct.2017.08.097>.
- [42] M. Świdziewski, M. Klasztorny, P. Dziewulski, P. Gotowicki, Numerical modelling, simulation and validation of the SPS and PS systems under 6 kg TNT blast shock wave, *Acta Mech. Autom.* 6 (2012) 77–87.
- [43] S.R.G. Bates, I.R. Farrow, R.S. Trask, 3D Printed Elastic Honeycombs With Graded Density for Tailorable Energy Absorption, 9799, 2016, 979907, <https://doi.org/10.1117/12.2219322>.
- [44] F.N. Habib, P. Iovenitti, S.H. Masood, M. Nikzad, In-plane energy absorption evaluation of 3D printed polymeric honeycombs, *Virtual Phys. Prototyp.* 12 (2017) 117–131, <https://doi.org/10.1080/17452759.2017.1291354>.
- [45] S. Soe, M. Ryan, G. McShane, P. Theobald, Energy Absorption Characteristics of Additively Manufactured TPE Cellular Structures, *Second Int. Conf. Sustain. Des. Manuf.* 2015 145–158 <http://orca.cf.ac.uk/id/eprint/73193>.
- [46] J. Stampfl, Regular, Low Density Cellular Structures - Rapid Prototyping, Numerical Simulation, Mechanical Testing, 823, 2004 1–6, <https://doi.org/10.1557/PROC-823-W8.8>.
- [47] M.H. Luxner, J. Stampfl, H.E. Pettermann, Numerical simulations of 3D open cell structures - influence of structural irregularities on elasto-plasticity and deformation localization, *Int. J. Solids Struct.* 44 (2007) 2990–3003, <https://doi.org/10.1016/j.ijsolstr.2006.08.039>.
- [48] Y.L. Yap, W.Y. Yeong, Shape recovery effect of 3D printed polymeric honeycomb: this paper studies the elastic behaviour of different honeycomb structures produced by PolyJet technology, *Virtual Phys. Prototyp.* 10 (2015) 91–99, <https://doi.org/10.1080/17452759.2015.1060350>.
- [49] D.M. Correa, T. Klatt, S. Cortes, M. Haberman, D. Kovar, C. Seepersad, Negative stiffness honeycombs for recoverable shock isolation, *Rapid Prototyp. J.* 21 (2015) 193–200, <https://doi.org/10.1108/RPJ-12-2014-0182>.
- [50] K. Wang, Y.H. Chang, Y. Chen, C. Zhang, B. Wang, Designable dual-material auxetic metamaterials using three-dimensional printing, *Mater. Des.* 67 (2015) 159–164, <https://doi.org/10.1016/j.matdes.2014.11.033>.
- [51] M.H. Fu, Y. Chen, L.L. Hu, A novel auxetic honeycomb with enhanced in-plane stiffness and buckling strength, *Compos. Struct.* 160 (2017) 574–585, <https://doi.org/10.1016/j.compstruct.2016.10.090>.
- [52] M.H. Fu, Y. Chen, L.L. Hu, Bilinear elastic characteristic of enhanced auxetic honeycombs, *Compos. Struct.* 175 (2017) 101–110, <https://doi.org/10.1016/j.compstruct.2017.04.007>.
- [53] T. Durejko, M. Zietala, W. Polkowski, T. Czujko, Thin wall tubes with Fe3Al/SS316L graded structure obtained by using laser engineered net shaping technology, *Mater. Des.* 63 (2014) 766–774, <https://doi.org/10.1016/j.matdes.2014.07.011>.
- [54] A. Ashab, D. Ruan, G. Lu, S. Xu, C. Wen, Experimental investigation of the mechanical behavior of aluminum honeycombs under quasi-static and dynamic indentation, *Mater. Des.* 74 (2015) 138–149, <https://doi.org/10.1016/j.matdes.2015.03.004>.
- [55] D. Mousanezhad, R. Ghosh, A. Ajdari, A.M.S. Hamouda, H. Nayeb-Hashemi, A. Vaziri, Impact resistance and energy absorption of regular and functionally graded

- hexagonal honeycombs with cell wall material strain hardening, *Int. J. Mech. Sci.* 89 (2014) 413–422, <https://doi.org/10.1016/j.ijmecsci.2014.10.012>.
- [56] ASTM, D638-14, Standard Test Method for Tensile Properties of Plastics, ASTM International, West Conshohocken, PA, 2014 www.astm.org.
- [57] ABSplus Spec Sheet, (n.d.). <http://www.stratasys.com/materials/fdm/absplus> (accessed June 8, 2017).
- [58] LS-DYNA Aerospace Working Group Modeling Guidelines Document, LS-DYNA Aerospace Working Group, https://awg.lstc.com/tiki/tiki-index.php?page=MGD_2017.
- [59] H. Lobo, Methodology for Selection of Material Models for Plastics Impact Simulation, 6th Eur. LS-DYNA Users' Conf., 2007 97–106.
- [60] H. Lobo, J.A. Hurtado, Characterization and Modeling of Non-linear Behavior of Plastics, 2006 ABAQUS Users' Conf., 2006 315–327.
- [61] J. Hallquist, LS-DYNA® theory manual, http://www.dynasupport.com/manuals/additional/ls-dyna-theory-manual-2005-beta/at_download/file 2006.
- [62] A.G. Hanssen, O.S. Hopperstad, M. Langseth, H. Iltstad, Validation of constitutive models applicable to aluminium foams, *Int. J. Mech. Sci.* 44 (2002) 359–406, [https://doi.org/10.1016/S0020-7403\(01\)00091-1](https://doi.org/10.1016/S0020-7403(01)00091-1).
- [63] P. Baranowski, K. Damaziak, J. Malachowski, L. Mazurkiewicz, A. Muszyński, A child seat numerical model validation in the static and dynamic work conditions, *Arch. Civ. Mech. Eng.* 15 (2015) 361–375, <https://doi.org/10.1016/j.acme.2014.07.001>.
- [64] P. Baranowski, J. Malachowski, L. Mazurkiewicz, Numerical and experimental testing of vehicle tyre under impulse loading conditions, *Int. J. Mech. Sci.* 106 (2016) 346–356, <https://doi.org/10.1016/j.ijmecsci.2015.12.028>.